Research article

NMR IN BIOMEDICINE

Received: 21 March 2016, Revised: 6 June 2016, Accepted: 7 June 2016, Published online in Wiley Online Library: 29 July 2016

(wileyonlinelibrary.com) DOI: 10.1002/nbm.3578

Towards longitudinal mapping of extracellular pH in gliomas

Yuegao Huang[a,b]*, Daniel Coman[a,b], Peter Herman[a,b], Jyotsna U. Rao[a,b], Samuel Maritim[c] and Fahmeed Hyder[a,b,c]*

Biosensor imaging of redundant deviation in shifts (BIRDS), an ultrafast chemical shift imaging technique, requires infusion of paramagnetic probes such as 1,4,7,10-tetraazacyclododecane-1,4,7,10-tetrakis methylene phosphonate ($DOTP^{8-}$) complexed with thulium (Tm^{3+}) ion (i.e. $TmDOTP^{5-}$), where the pH-sensitive resonances of hyperfine-shifted non-exchangeable protons contained within the paramagnetic probe are detected. While imaging extracellular pH (pH_e) with BIRDS meets an important cancer research need by mapping the intratumoral–peritumoral pH_e gradient, the surgical intervention used to raise the probe's plasma concentration limits longitudinal scans on the same subject. Here we describe using probenecid (i.e. an organic anion transporter inhibitor) to temporarily restrict renal clearance of $TmDOTP^{5-}$, thereby facilitating molecular imaging by BIRDS without surgical intervention. Co-infusion of probenecid with $TmDOTP^{5-}$ increased the probe's distribution into various organs, including the brain, compared with infusing $TmDOTP^{5-}$ alone. *In vivo* BIRDS data using the probenecid–$TmDOTP^{5-}$ co-infusion method in rats bearing RG2, 9 L, and U87 brain tumors showed intratumoral–peritumoral pH_e gradients that were unaffected by the probe dose. This co-infusion method can be used for pH_e mapping with BIRDS in pre-clinical models for tumor characterization and therapeutic monitoring, given the possibility of repeated scans with BIRDS (e.g. over days and even weeks) in the same subject. The longitudinal pH_e readout by the probenecid–$TmDOTP^{5-}$ co-infusion method for BIRDS adds translational value in tumor assessment and treatment.

Additional supporting information may be found in the online version of this article at the publisher's web site.

Keywords: CEST; extravasation; metastasis; permeability; renal ligation; uric acid reducer

INTRODUCTION

Gliomas are the most common central nervous system tumors (1,2). Tumor cells exhibit increased glucose uptake and elevated lactate generation despite presence of sufficient oxygen for oxidative phosphorylation. This phenomenon is known as aerobic glycolysis, but it is also referred to as the Warburg effect after its discoverer (3). Elevated aerobic glycolysis of tumor cells generates excessive protons (and other acids), which have to be excreted out of the cell, and as a result the extracellular pH (pH_e) becomes acidic in most solid tumors. Given that pH_e for normal tissue is close to neutral, the pH_e inside and outside tumor core can differ, thereby generating an intratumoral–peritumoral pH_e gradient. Extracellular acidosis promotes tumor growth, cell invasion, metastasis, and resistance to therapy (4–6). Thus, mapping the intratumoral–peritumoral pH_e gradient quantitatively is an important biomarker in tumor diagnosis and prognosis after treatment (7,8).

Noninvasive MR methods are ideal for cancer imaging, and various tumor properties have been targeted, e.g. diffusion or perfusion (9–11). In particular, pH_e mapping is possible with both MRI – e.g. contrast based on relaxation or chemical exchange – and MRS (12–14). Biosensor imaging of redundant deviation in shifts (BIRDS) is an ultrafast chemical shift imaging (CSI) platform for molecular imaging in which paramagnetically shifted non-exchangeable protons (i.e. CH_x) on DOTA-based macrocyclic complexes are directly detected (15–21). BIRDS has some unusual properties. Both longitudinal (T_1) and transverse (T_2) relaxation times of protons of the complexes are very short (i.e. only in the ms range) due to their close proximity to the paramagnetic metal ion. Short T_1 allows fast averaging, whereas short T_2 means insensitivity to static magnetic field inhomogeneity. T_2 and T_1 equivalence leads intrinsically to higher MR sensitivity. Because the proton resonances of the agent are sufficiently shifted away from the water proton resonance, there are no overlaps with signals from other metabolites. Finally, the pH_e

* *Correspondence to: Y. Huang, Magnetic Resonance Research Center, Yale University, New Haven, CT, USA. E-mail: yuegao.huang@yale.edu*
F. Hyder, Department of Biomedical Engineering, Yale University, New Haven, CT, USA.

a *Y. Huang, D. Coman, P. Herman, J. U. Rao, F. Hyder*
Magnetic Resonance Research Center, Yale University, New Haven, CT, USA

b *Y. Huang, D. Coman, P. Herman, J. U. Rao, F. Hyder*
Department of Radiology and Biomedical Imaging, Yale University, New Haven, CT, USA

c *S. Maritim, F. Hyder*
Department of Biomedical Engineering, Yale University, New Haven, CT, USA

Abbreviations used: *ASL, arterial spin labeling; BIRDS, biosensor imaging of redundant deviation in shifts; CEST, chemical exchange saturation transfer; CSI, chemical shift imaging; $DOTP^{8-}$, 1,4,7,10-tetraazacyclododecane-1,4,7,10-tetrakis methylene phosphonate; FOV, field of view; FWHM, full width at half maximum; OAT, organic anion transporter; pH_e, extracellular pH; SNR, signal to noise ratio.*

readout does not depend on the agent concentration because the readout is purely based on shift changes (i.e. not peak heights).

Previously we reported the feasibility of using DOTA phosphonates (e.g., $TmDOTP^{5-}$ and TmDOTA-4AmP^{5-}) to map the intratumoral–peritumoral pH_e gradient of brain tumors (22). However, to raise the concentration of the agents in brain tissue, we surgically stopped renal clearance of the agents. While this method provided sufficient local concentration of agents for molecular imaging, it required surgical intervention – thus preventing longitudinal survival studies.

Probenecid inhibits organic anion transporters (OATs) and it has been used clinically to decrease the renal excretion of drugs, such as penicillin, bumetanide, and zidovudine (23–25). While probenecid can be used as an adjuvant agent to increase the systemic level of drugs, it also serves as an OATs3 inhibitor, mediating efflux of drugs across the blood–brain barrier (26). Hence, probenecid can significantly increase drug concentration in plasma and target tissues for prolonged treatment. For example, the distribution of fluorescein in brain was enhanced twofold when probenecid was co-administered with the drug (27). Probenecid has a half-life of 4–12 h (28), and although the effect is temporary it allows sufficient time for imaging. We hypothesized that pH_e imaging of gliomas with BIRDS can be achieved when probenecid and $TmDOTP^{5-}$ are co-infused. We show that the co-infusion method is safe and fast, and thus is a viable alternative to renal ligation for BIRDS. Thus, longitudinal monitoring of tumor growth and assessment of therapeutic response will be possible with the probenecid–$TmDOTP^{5-}$ co-infusion method for BIRDS.

MATERIALS AND METHODS

Probenecid was purchased from Sigma-Aldrich (St. Louis, MO, USA) and $TmDOTP^{5-}$ was obtained from Macrocyclics (Dallas, TX, USA). Tumor cell lines RG2, 9 L, and U87 were purchased from American Type Culture Collections (Manassas, VA, USA). Adult male Sprague-Dawley rats (200–250 g), male Fischer 344 rats (200–250 g), and nude rats (150–200 g) were obtained from Yale University vendors and maintained according to approved animal care protocols. All animal experiments were performed under NIH guidelines and approved by the institutional animal care and use committee (IACUC) at Yale University. *In vivo* MR scans were conducted on an 11.7 T Agilent (Santa Clara, CA, USA) horizontal-bore spectrometer (bore size = 21 cm; maximum gradient strength = 400 mT/m) using a custom built ^{1}H surface RF probe (1.4 cm diameter). *Ex vivo* samples were scanned on an 11.7 T Bruker (Billerica, MA, USA) vertical-bore spectrometer.

Biodistribution and survival experiments

Sprague-Dawley rats were anesthetized with isoflurane (~2%). A femoral vein and an artery were cannulated for agent/drug infusion and physiological monitoring (pCO_2, pO_2, pH, and blood pressure) during the experiment, respectively. Rats were separated into three groups and in each group we infused either 0.1 or 1 mmol/kg $TmDOTP^{5-}$ for 120 min ($n = 6$ in each case). In Group I we infused $TmDOTP^{5-}$ (0.1 and 1 mmol/kg) without probenecid or renal ligation. In Group II we co-infused $TmDOTP^{5-}$ (0.1 and 1 mmol/kg) and probenecid (100 mg/kg). In Group III we infused $TmDOTP^{5-}$ (0.1 and 1 mmol/kg) after renal ligation. The concentration of probenecid stock solution was 100 mg/mL at pH 7.4. The concentrations of the $TmDOTP^{5-}$ stock solutions were 150 mM and 15 mM for 1 mmol/kg and 0.1 mmol/kg doses, respectively, dissolved in 100 mg/kg probenecid. The infusion rate was 15 μL/min for probenecid and $TmDOTP^{5-}$.

Blood plasma and urine samples were collected throughout the experiment from rats in Groups I and II. Plasma concentrations were used for calibrating the agent concentration in the tissue using tissue–plasma volumes (29). After the infusion, rats were euthanized with focused microwave irradiation (30), immediately after which various organs (i.e. brain cortex and subcortex, lung, heart, liver, spleen, muscle, and kidney) were removed, weighed, and homogenized for agent concentration analysis by ^{1}H NMR. We used 0.1 mM $TmDOTMA^-$ as an internal reference. NMR spectra were collected using standard pulse–acquire experiments on an 11.7 T vertical-bore magnet using fast acquisition times and the intensity of the H6 proton of $TmDOTP^{5-}$ was measured. The final tissue concentrations of $TmDOTP^{5-}$ were calculated after reference and plasma corrections.

A few rats ($n = 4$) were anesthetized (~2% isoflurane) and the tail vein was cannulated for co-infusion of $TmDOTP^{5-}$ (1 mmol/kg) and probenecid (100 mg/kg) for 120 min. A water-heating pad maintained the body temperature in the physiological range (36–37 °C). The rats were survived after the co-infusion. The rats' activity (e.g. sleep and eating cycles) was monitored for 48 h before the co-infusion study was repeated and then revived again.

Tumor rat preparation

RG2 and 9 L cells were cultured in T75 flasks in DMEM media containing 10% heat inactivated FBS and 1% antibiotics at 37 °C and 5% CO_2, whereas U87 cells were cultured in T75 flasks in MEM media containing 10% heat inactivated FBS and 1% antibiotics at 37 °C and 5% CO_2.

Tumor cells were harvested at 60–80% confluence, washed and suspended in serum-free media for implantation in Fischer 344 rats (5 μL 2×10^4 RG2 cells and 5 μL 1×10^5 9 L cells) and nude rats (5 μL 5×10^5 U87 cells). Rats were anesthetized with isoflurane (~2%) and positioned in a stereotaxic system. A water-heating pad was used to maintain the body temperature in the physiological range (36–37 °C). Tumor cells were injected with a 25 μL Hamilton syringe into the right thalamus at coordinates 3 mm laterally to the right of the bregma and 3 mm ventral to the dura. A 5 μL volume of the cell suspension was injected over the course of 5 min and the needle was left in place for an additional 5 min before slow withdrawal.

On the day of scanning, rats ($n = 6$ for RG2 and 9 L tumors each and $n = 3$ for U87 tumor) were anesthetized (~2% isoflurane), tracheotomized, and artificially ventilated (70% N_2O–30% O_2). A femoral vein and an artery were cannulated for agent/drug infusion and physiological monitoring (pCO_2, pO_2, pH, and blood pressure) during the experiment. A water-heating pad was used to maintain the body temperature in the physiological range (36–37 °C) throughout the experiment. Body temperature was measured with a rectal probe and no further adjustments in the water-heating pad were made for the entire duration of the experiment (~150 min). Probenecid (100 mg/kg) and $TmDOTP^{5-}$ (1 mmol/kg) were co-infused for a maximum of 120 min.

BIRDS data analysis

Spin-echo MRI datasets (128 × 128 resolution, 1 mm slice thickness, field of view (FOV) 25 × 25 mm^2, recycle time (T_R) 6 s, echo

time (T_E) 10 ms) were obtained for tumor localization and visualization. *In vivo* 3D CSI for BIRDS data were acquired 30 min after probenecid–TmDOTP^{5-} co-infusion began, using a dual-banded refocused 90° Shinnar–Le Roux RF pulse (35 kHz bandwidth and 90 kHz separation with 205 μs duration) for selective excitation of the H2/H3 and H6 protons of TmDOTP^{5-}. The 3D CSI datasets were acquired with a T_R of 5 ms and an FOV of $25 \times 25 \times 25$ mm^3, a spectral window of 250 kHz and the acquisition time of 4.1 ms. The total time of each 3D CSI dataset acquisition was 12 min. The 3D CSI data were reconstructed to $25 \times 25 \times 25$ resolution, resulting in a nominal voxel resolution of 1 μL. Each ^{1}H spectrum was line broadened (500 Hz), phased (zero order), and baseline corrected (first order). The data were analyzed in MATLAB (MathWorks, Natick, MA, USA). The pH for each voxel was calculated from the chemical shifts of the H2, H3, and H6 protons of TmDOTP^{5-} according to

$$\mathrm{pH} = a_0 + \sum_{k=2,3,6} a_1^k \delta_k + \sum_{k=2,3,6} \sum_{j=2,3,6} a_2^{kj} \delta_k \delta_j \qquad [1]$$

where the coefficients a_0, a_1^k, and a_2^{kj} were calculated from linear least-squares fit of pH as a function of chemical shifts δ_2, δ_3, and δ_6, as previously described (22). The tumor and its margin were localized by MRI contrast and pH$_e$ measured by BIRDS was assessed for voxels inside the tumor (intratumoral) and outside the tumor (peritumoral). Intratumoral and peritumoral voxels were defined as all voxels inside and outside the tumor boundary defined by MRI, respectively. Voxels that were partly inside or outside the tumor were excluded in the analysis. For single voxel region-of-interest analysis, an intratumoral voxel was selected in the center of the tumoral voxels and compared with a contralateral peritumoral voxel. The significance between intratumoral and peritumoral pH$_e$ was assessed by Student's *t*-test, where *P*-values less than 0.05 were considered to be significant.

RESULTS

Probenecid is a non-selective OAT inhibitor used to raise the plasma concentrations of drugs (31). We examined the effect of probenecid–TmDOTP^{5-} co-infusion in rats. Plasma concentration was higher for probenecid–TmDOTP^{5-} co-infusion than TmDOTP^{5-} infusion alone (Fig. S1), but the highest plasma concentration was achieved for infusion with renal ligation. In contrast, urine concentration was lower for probenecid–TmDOTP^{5-} co-infusion than TmDOTP^{5-} infusion alone. These results suggest that probenecid inhibited the renal clearance of TmDOTP^{5-}.

Biodistribution data of TmDOTP^{5-} in the rat's body is presented in Figs. 1 and S2. TmDOTP^{5-} concentrations in various organs (brain cortex, brain subcortex, liver, lung, heart, muscle,

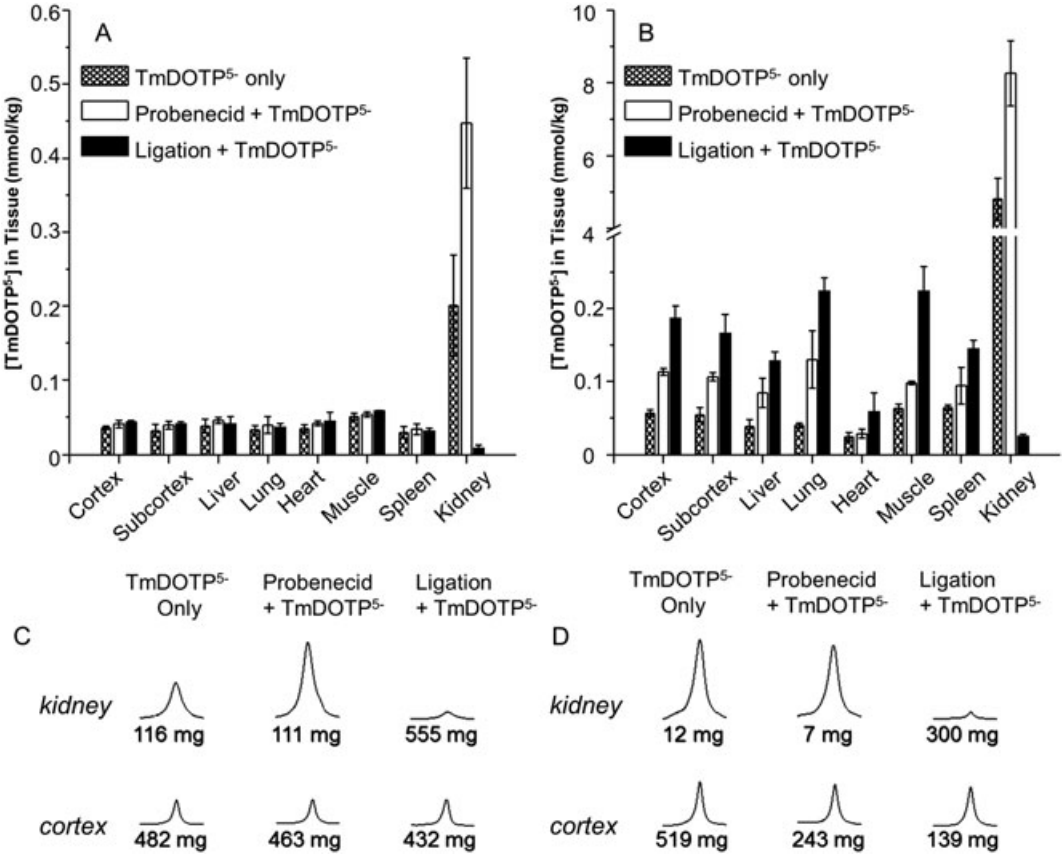

Figure 1. Biodistribution of TmDOTP^{5-} in the rat body. (A, B) Summary of TmDOTP^{5-} biodistribution (mmol/kg) in rats that were infused with (A) 0.1 mmol/kg TmDOTP^{5-} and (B) 1 mmol/kg TmDOTP^{5-} in three experimental conditions: infusion of TmDOTP^{5-} alone, co-infusion of 100 mg/kg probenecid and TmDOTP^{5-}, and infusion of TmDOTP^{5-} in renal ligated rats. (C, D) Representative spectra of the H6 proton in TmDOTP^{5-} from the kidney and cortex samples of rats that were infused with (C) 0.1 mmol/kg TmDOTP^{5-} and (D) 1 mmol/kg TmDOTP^{5-}. The weight of each tissue sample is indicated below the corresponding spectrum. The concentration of TmDOTP^{5-} in each sample was estimated by the intensity of each spectrum after reference and plasma corrections.

spleen, and kidney) were quantitatively measured and compared for the three different infusion protocols: infusion of $TmDOTP^{5-}$ without any intervention, co-infusion of $TmDOTP^{5-}$ with probenecid, and $TmDOTP^{5-}$ infusion with renal ligation.

Two infusion doses of $TmDOTP^{5-}$ were used. At low dose of 0.1 mmol/kg (Fig. 1A), $TmDOTP^{5-}$ concentrations in tissues for the co-infusion method were slightly higher than for infusion of $TmDOTP^{5-}$ alone, but comparable to $TmDOTP^{5-}$ concentrations detected using the renal ligation method. The enhancement in $TmDOTP^{5-}$ concentration in various tissues is small at low dose and becomes larger at high dose with both co-infusion and ligation methods. At the high dose of 1 mmol/kg (Fig. 1B), the differences in $TmDOTP^{5-}$ concentration in each tissue for the three infusion methods were larger. As noted by the H6 intensities in $TmDOTP^{5-}$ depicted in Figs. 1C, D, co-infusion of $TmDOTP^{5-}$ with probenecid increased $TmDOTP^{5-}$ concentrations in both kidney and brain. Rats revived after co-infusion of $TmDOTP^{5-}$ with probenecid showed no overt behavioral signs that were different from rats revived from anesthesia. Although the probenecid–$TmDOTP^{5-}$ co-infusion method did not result in an increase of $TmDOTP^{5-}$ concentration in the tissue as remarkably as the renal ligation method, it was approximately double that with infusion of $TmDOTP^{5-}$ alone. Therefore, co-infusion of $TmDOTP^{5-}$ with probenecid provides a good alternative to renal ligation to raise the $TmDOTP^{5-}$ concentration in various tissues, including brain.

Representative BIRDS data of a brain bearing an RG2 tumor in a Fischer rat after co-infusion of $TmDOTP^{5-}$ with probenecid are shown in Fig. 2. T_2-weighted MRI identified the tumor upon $TmDOTP^{5-}$ infusion (Fig. 2A). The tumor region was slightly darkened by T_2 contrast as a result of $TmDOTP^{5-}$ extravasation due to higher permeability of the tumor vasculature. While the tumor border may not be clearly distinguishable by endogenous MRI contrast (see, e.g., Fig. S2 in Reference 22), endogenous MRI contrast is needed for arterial spin labeling (ASL) to measure blood flow differences within and beyond tumor boundary. Future studies with ASL and BIRDS in the same subject will provide novel relations between gradients of intratumoral–peritumoral blood flow and pH_e. The $TmDOTP^{5-}$ CSI dataset in Fig. 2B shows the resonances H2, H3, and H6 of $TmDOTP^{5-}$ in intratumoral and peritumoral voxels. pH_e values of each voxel were differentially determined by chemical shifts of $TmDOTP^{5-}$ resonances according to Equation [1]. As an example, a selected intratumoral voxel ($\delta_2 = 58.96$ ppm, $\delta_3 = 76.97$ ppm, and $\delta_6 = -141.09$ ppm) had a pH_e of 6.64 (Fig. 2C) and a selected peritumoral voxel ($\delta_2 = 59.75$ ppm, $\delta_3 = 77.52$ ppm, and $\delta_6 = -140.42$ ppm) had a pH_e of 7.27 (Fig. 2D). Consistent with our previous results, the intratumoral pH_e values were distinctly lower than peritumoral pH_e values for rat brains bearing RG2 tumors (22). In this rat brain with an RG2 tumor, the average pH_e values of intratumoral voxels were 6.73 ± 0.02 while those of peritumoral voxels were 7.11 ± 0.01. We showed previously that the large intratumoral–peritumoral pH_e gradient for aggressive tumors (e.g. RG2 versus 9 L) matched the increased presence of Ki-67 (proliferation marker) positive cells beyond the tumor border (see Figs. 1 and S1 in Reference 22).

The overall intensities of proton resonances for intratumoral voxels were higher than those for peritumoral voxels, indicating higher $TmDOTP^{5-}$ accumulation in the intratumoral region of the RG2 tumor. As an example shown in Fig. 3A, the intensity of the H6 proton resonance of a selected intratumoral voxel was higher than that of a selected peritumoral voxel. Intensities of the resonances across the brain increased during co-infusion. However, the concentration decreased at latter stages of the co-infusion, suggesting agent clearance. In support of this, both urine and plasma signals showed a decrease of $TmDOTP^{5-}$ signal immediately after the end of infusion (Fig. S1). Although the intensities of each resonance of $TmDOTP^{5-}$ varied across either intratumoral or peritumoral voxels, pH_e determination by BIRDS was independent of $TmDOTP^{5-}$ concentration. Thus, even though a lower concentration of $TmDOTP^{5-}$ was present in the peritumoral region, the pH_e of each voxel was accurately determined. As shown in Figs. 3B, C, the pH_e maps obtained about 12 min apart during the probenecid–$TmDOTP^{5-}$ co-infusion were nearly identical, indicating dose-independent pH_e imaging with BIRDS. The correlation between these two pH_e maps was excellent (Fig. S3).

Probenecid–$TmDOTP^{5-}$ co-infusion was tested in rats bearing different types of glioma (Fig. 4). More aggressive xenograft U87 tumors and less aggressive gliosarcomas 9 L were similarly localized using T_2-weighted MRI images (Figs. 4A(i) and 4B(i), respectively). The $TmDOTP^{5-}$ CSI datasets for U87 and 9 L tumors with probenecid–$TmDOTP^{5-}$ co-infusion showed higher signals inside the tumor core (Figs. 4A(ii) and 4B(ii)). The pH_e map of the U87 tumor showed low values in the intratumoral region as well as the tumor margin (Fig. 4A(iii)), whereas the pH_e map of the 9 L

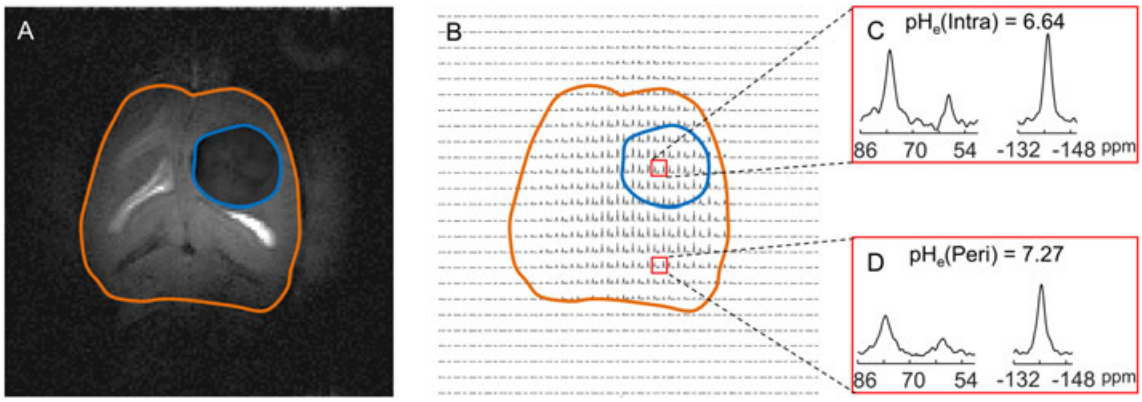

Figure 2. Representative MRI and BIRDS data from a rat bearing an RG2 tumor during probenecid–$TmDOTP^{5-}$ co-infusion. (A) A T_2-weighted image shows the tumor localization due to agent extravasation (blue outline, tumor; orange outline, brain). (B) A slice from a 3D CSI dataset shows varying $TmDOTP^{5-}$ levels throughout the brain (the same slice as in A). (C) Examples of $TmDOTP^{5-}$ resonances, which indicate that the pH_e (according to Equation [1]) of an intratumoral voxel ($pH_e = 6.64$) is lower than that of a peritumoral voxel ($pH_e = 7.27$).

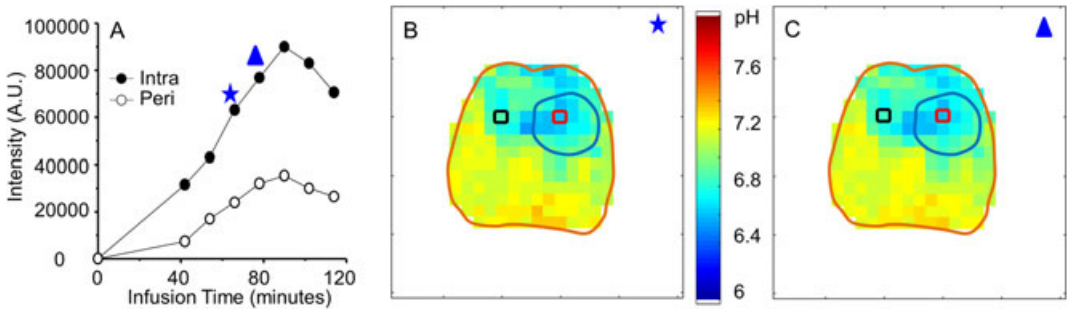

Figure 3. pH_e maps by BIRDS are independent of $TmDOTP^{5-}$ concentration. (A) Resonance intensities of H6 in $TmDOTP^{5-}$ for intratumoral (red boxes in pH_e maps in B and C) and peritumoral (black boxes in pH_e maps in B and C) voxels at various time points during co-infusion of $TmDOTP^{5-}$ with probenecid. (B, C) Quantitative pH_e maps (according to Equation [1]) obtained at different $TmDOTP^{5-}$ concentrations indicated by stars and triangles respectively at (B) 66 min and (C) 78 min after the start of probenecid–$TmDOTP^{5-}$ co-infusion. See Fig. S3 for correlation of these pH_e maps.

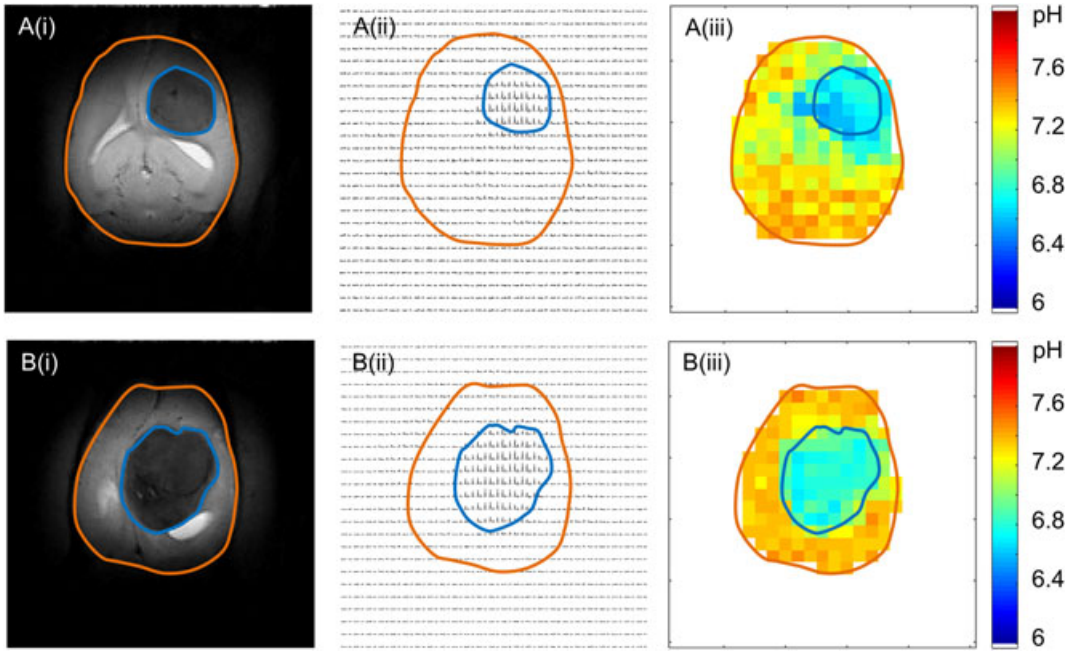

Figure 4. Representative MRI and BIRDS data of rats bearing U87 and 9 L tumors during probenecid–$TmDOTP^{5-}$ co-infusion. The left-hand column shows the T_2-weighted images, which depict the localized (A) U87 and (B) 9 L tumors, due to agent extravasation (blue outline, tumor; orange outline, brain). The middle column shows a representative slice from 3D CSI datasets showing varying $TmDOTP^{5-}$ levels throughout the brain of (A) U87 and (B) 9 L tumors. The right-hand column shows the pH_e maps (according to Equation [1]) calculated from $TmDOTP^{5-}$ resonances in (A) U87 and (B) 9 L tumors. Figure 2 shows similar data for an RG2 tumor.

tumor showed low values in the intratumoral region and high values in the peritumoral region (Fig. 4B(iii)).

The intratumoral and peritumoral pH_e values for each tumor type measured by BIRDS are summarized in Fig. 5. The histograms were fitted to a Gaussian distribution to obtain the most probable (or expected) pH_e value and the full width at half maximum, FWHM (Table 1). The results show that the intratumoral–peritumoral pH_e gradients of brains with 9 L and U87 tumors were larger than those of brains bearing RG2 tumors, suggesting that the pH_e boundary between intratumoral and peritumoral regions was clearer for 9 L and U87 tumors.

For brains bearing 9 L tumors (Fig. 5A), the expected pH_e values of intratumoral and peritumoral regions were 6.84 ± 0.01 and 7.32 ± 0.01, respectively, indicating that the intratumoral–peritumoral pH_e gradient was about 0.5. However the FWHM of the intratumoral distribution (0.24 ± 0.01) was similar to that of the peritumoral distribution (0.25 ± 0.01), indicating that the pH_e values were homogeneous in the two regions. Thus the pH_e boundary between intratumoral and peritumoral regions was well resolved for 9 L tumors (Table 1).

For brains with U87 tumors (Fig. 5B), the expected pH_e values of intratumoral and peritumoral regions were 6.84 ± 0.02 and 7.34 ± 0.02, respectively, indicating that the intratumoral–peritumoral pH_e gradient was again about 0.5. However, the FWHM of the intratumoral distribution (0.37 ± 0.02) was larger than that of the peritumoral distribution (0.20 ± 0.01), indicating that the pH_e values in intratumoral voxels were more spread. Thus the pH_e boundary for U87 tumors was more heterogeneous than that for 9 L tumors (Table 1).

For brains with RG2 tumors (Fig. 5C), the expected pH_e values of intratumoral and peritumoral regions were 6.83 ± 0.02 and 7.22 ± 0.01, respectively, indicating that the intratumoral–

NMR IN BIOMEDICINE

Table 1. Most probable pH_e values and the FWHM obtained from the fit of the normal (Gaussian) distribution of pH_e shown in Fig. 5 for intratumoral and peritumoral regions in 9 L, U87, and RG2 tumors. See Fig. S4 for the relation between tumor size and tumor pH_e

Region	9 L		U87		RG2	
	pH_e	FWHM	pH_e	FWHM	pH_e	FWHM
Intratumoral pH_e	6.84 ± 0.01	0.24 ± 0.01	6.81 ± 0.02	0.37 ± 0.02	6.83 ± 0.02	0.17 ± 0.01
Peritumoral pH_e	7.32 ± 0.01	0.25 ± 0.01	7.34 ± 0.01	0.20 ± 0.01	7.22 ± 0.01	0.42 ± 0.03
Intratumoral–peritumoral pH_e gradient	0.48 ± 0.01	–	0.53 ± 0.02	–	0.39 ± 0.02	–
Tumor size (μL)	111.7 ± 37.7	–	68.1 ± 17.6	–	83.9 ± 35.7	–

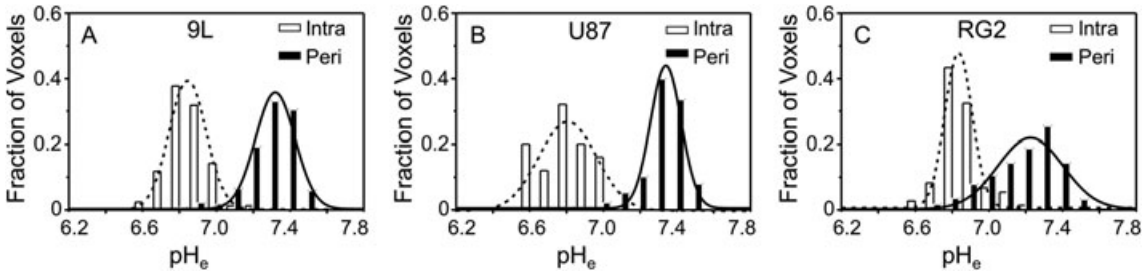

Figure 5. Distributions of intratumoral and peritumoral pH_e values. Histograms representing the distribution of intratumoral and peritumoral pH_e measured by BIRDS for (A) 9 L, (B) U87, and (C) RG2 tumors. The fraction of voxels with a given pH_e value is shown for intratumoral voxels and peritumoral voxels.

peritumoral pH_e gradient was about 0.4 for RG2 tumors. Moreover, the FWHM of the intratumoral distribution (0.17 ± 0.01) was smaller than that of the peritumoral distribution (0.42 ± 0.03), and the peritumoral distribution overlaps partially with the intratumoral distribution, indicating that low pH_e values were measured in peritumoral regions. Thus the pH_e boundary between intratumoral and peritumoral regions was not clear for RG2 tumors (Table 1).

Because different tumors grow at different rates, we could not image all tumor types at the same size. We have estimated the tumor volume for each tumor type (9 L, 111.7 ± 37.7 μL; RG2, 83.9 ± 35.7 μL; U87, 68.1 ± 17.6 μL). The measured intratumoral pH_e was independent of tumor volume (Table 1; Fig. S4). However it should be noted that the peritumoral pH_e also changes for aggressive tumors (22). For each given tumor cell line, the pH_e values were statistically significant between intratumoral and peritumoral voxels ($p < 0.05$). For intratumoral pH_e, an ANOVA showed that there were significant differences across three tumor types ($p = 0.011$); a post hoc Bonferroni test revealed significant differences between 9 L and U87 tumors ($p = 0.023$), and between RG2 and U87 tumors ($p = 0.019$). For peritumoral pH_e, an ANOVA showed that there was significant differences across three tumor types ($p = 0.000$); a post hoc Bonferroni test revealed significant differences between 9 L and RG2 tumors ($p = 0.000$), and between RG2 and U87 tumors ($p = 0.019$).

DISCUSSION

Acidic pH_e is one of the primary cancer hallmarks and thus a target for cancer imaging (32). Mapping intratumoral and peritumoral pH_e with BIRDS is valuable in assessing both tumor growth and possible therapeutic response. Previous work with BIRDS has shown promise for pH_e mapping of brain tumors (22). The urinary excretion is the major pathway to eliminate most MRI contrast agents, including $TmDOTP^{5-}$. Thus, to inhibit rapid clearance of $TmDOTP^{5-}$, previous BIRDS imaging required surgical intervention (i.e. renal ligation) to raise the agent's concentration in the plasma as well as in the tissue. Longitudinal monitoring of pH_e using BIRDS on tumors is an unmet need and could be achieved if the renal system is only temporarily (and not permanently) inhibited. Probenecid has been widely used to temporarily decrease the renal clearance of drugs. Hence, probenecid can be used as an alternative to renal ligation to allow longitudinal assessment of tumor microenvironments with BIRDS.

Compared with conventional water-based proton MRI, BIRDS is a molecular imaging technique that detects non-exchangeable protons on the paramagnetic agent in response to variations in microenvironment. Because BIRDS readouts rely on the chemical shift changes of hyperfine-shifted proton resonance, the molecular sensitivity is independent of the agent's concentration, without any background overlapping signals. Moreover, BIRDS does not interfere with the conventional water-based proton MRI method; for example, BIRDS signals and sensitivities are not affected by the presence of superparamagnetic iron oxide or even gadolinium-based contrast agents (21), which are widely used to localize brain tumors in patients.

Tissue distribution of $TmDOTP^{5-}$ is the key to successful BIRDS experiments. Probenecid was efficient to raise the plasma and tissue concentrations of $TmDOTP^{5-}$ in the infusion dose range of 0.1–1 mmol/kg (Figs. 1A, B). While $TmDOTP^{5-}$ concentrations in kidney were higher for the co-infusion method than for $TmDOTP^{5-}$ infusion alone (Figs. 1C, D), $TmDOTP^{5-}$ concentrations in brain cortex were slightly higher for co-infusion and ligation methods compared with infusion of $TmDOTP^{5-}$ alone. As the infusion dose increased, biodistribution data showed that the enhancement in tissue concentrations for the probenecid–$TmDOTP^{5-}$ co-infusion method was more noticeable, although the non-survival renal

ligation method results in higher tissue concentrations. In addition, the effect was universal and non-selective for specific organs, including the brain. Delivery of $TmDOTP^{5-}$ to the brain is in general more difficult than that to other organs because the blood–brain barrier prevents the agent entering the brain readily (33). Thus, a non-surgical method (i.e. probenecid–$TmDOTP^{5-}$ co-infusion) that can increase the life-time of the agent in the blood circulation and thus raise the concentration of the agent in the brain is preferable. With the high signal-to-noise ratio (SNR) detected for the protons at the current $TmDOTP^{5-}$ dose used for BIRDS data, it seems that even lower $TmDOTP^{5-}$ dose can be used in the future with the co-infusion method.

Probenecid-mediated elevated agent concentration in brain tissue can be attributed to inhibition of OATs in both kidney and brain (34). Thus, probenecid markedly increased $TmDOTP^{5-}$ concentration in brain, most probably by two mechanisms: increased plasma concentration and/or half-life of $TmDOTP^{5-}$ by inhibition of $TmDOTP^{5-}$ excretion in the kidney, and reduced $TmDOTP^{5-}$ elimination by inhibition of OATs (35,36). More experiments are required to further illustrate the mechanism of probenecid-mediated $TmDOTP^{5-}$ enhancement in tissues. Other OATs inhibitors (e.g. sulfinpyrazone and benzbromarone) could possibly be used to enhance tissue concentration of $TmDOTP^{5-}$ (37,38).

A tumor has immature (i.e. leaky) vascular structure, which may facilitate the permeability of the contrast agent into the tumor, and poor perfusion may increase the retention time (3). The strong T_2-weighted contrast observed due to higher accumulation of $TmDOTP^{5-}$ in the tumor was consistent with our previous study when renal ligation was used (22). Using probenecid–$TmDOTP^{5-}$ co-infusion, a higher concentration of $TmDOTP^{5-}$ was observed for intratumoral voxels compared with peritumoral voxels, as shown by their MR resonance intensities (Fig. 3). *Ex vivo* quantitative analysis agreed with the *in vivo* results, showing that the intratumoral region had higher $TmDOTP^{5-}$ concentration (0.36 ± 0.02 mmol/kg) compared with the peritumoral region (0.13 ± 0.02 mmol/kg). In addition, the concentrations in both intratumoral and peritumoral regions with probenecid–$TmDOTP^{5-}$ co-infusion were higher than with a similar infusion dose of $DyDOTP^{5-}$ without probenecid (14).

A typical experiment of pH_e mapping with BIRDS using probenecid–$TmDOTP^{5-}$ co-infusion was acquired within 12 min. We demonstrated in our previous work (with renal ligation) that for typical *in vivo* detection of $TmDOTP^{5-}$ protons (i.e. H2, H3, and H6) with SNR of 15 the error in the pH_e measurement was 0.0013 (18). Although the SNR is slightly lower in these newer experiments (17,22), the estimation of pH_e error is still less than 0.01. pH_e maps acquired at different time points of co-infusion and therefore corresponding to different $TmDOTP^{5-}$ doses (Figs. 3B, C) were very similar. This observation is presented in Fig. S3 by plotting pH_e maps obtained about 12 min apart. The plot has a slope equal or close to unity, suggesting the reliability of the BIRDS method and the dose-independent pH_e mapping with BIRDS using probenecid–$TmDOTP^{5-}$ co-infusion. In addition, we validated pH readout with BIRDS for $TmDOTP^{5-}$ samples containing BSA with measurements from a pH electrode, where the comparison showed excellent agreement for pH within the physiological range (Fig. S5). For future experiments, improved SNR for BIRDS can be achieved by shorter acquisition times through hardware improvement (e.g. faster digitizer) and alternative pulse sequence design (e.g. ultrashort T_E sequences) (39). Methylated BIRDS agents could be synthesized to provide significant SNR increase (17). In addition, these paramagnetic agents also have exchangeable protons ($-NH_y$), which can be used for chemical exchange saturation transfer (CEST) imaging to provide higher spatial resolution images and multi-modality with BIRDS (16,19). Furthermore, hypoxia (i.e. low pO_2) is also a hallmark of tumor microenvironment. Simultaneous imaging of pH_e and pO_2 with BIRDS is possible when both pH_e- and pO_2-sensitive chelates are attached to the cyclen-based probes (40,41).

Three tumor models (i.e. RG2 as a glioblastoma, 9 L as a gliosarcoma, and U87 as a human glioblastoma multiforme xenograft) were used in this study to test the probenecid–$TmDOTP^{5-}$ co-infusion method for pH_e mapping with BIRDS. All three tumor models have been widely studied for cancer imaging as they are good models to represent human-like gliomas (42). While 9 L tumors are considered aggressive and infiltrative, RG2 and U87 tumors are more invasive models, mimicking human high-grade gliomas. However, microvessel studies by MRI and metabolite profiling by proton MRS show large variations in tumor properties, and thus are incapable of distinguishing among tumor models (43,44). Simultaneous pH_e measurements inside and outside the tumor core using the probenecid–$TmDOTP^{5-}$ co-infusion method enabled mapping of the intratumoral–peritumoral pH_e gradient, which may serve as an additional biomarker for tumor assessment, but also in monitoring the efficiency of tumor treatment over longitudinal studies in the same subject.

Tumor acidosis promotes invasion and resistance to therapy (45,46). The Warburg effect is believed to be the major mediator of the low pH_e observed in the tumor microenvironment. In addition, poor perfusion in tumors, which causes ineffective removal of excess H^+ and lactate, cannot be neglected. Gillies and coworkers demonstrated that low pH_e of the tumor drives local invasion (6). H^+ ions generated by tumor cells diffuse into adjacent normal tissues, causing tissue remodeling and promoting invasion. Various MR methods, including ^{31}P MRS, T_1- and T_2-based MRI, and CEST imaging, have been proposed for tumor imaging of pH_e (8,14,47,48). However, these methods mainly focus on intratumoral regions. Our previous study showed that intratumoral–peritumoral pH_e gradient was smaller in RG2 tumors than in 9 L tumors (22), suggesting RG2 tumors demonstrate more invasive features. In agreement with previous studies, here we also measured an intratumoral pH_e lower than the peritumoral pH_e and therefore the intratumoral–peritumoral pH_e gradient was smaller in more invasive RG2 tumors. pH_e mapping with BIRDS provides a clear picture regarding the invasive properties of aggressive tumors by showing low pH_e in peritumoral voxels. Although the intratumoral–peritumoral pH_e gradient of U87 tumors was similar to that of 9 L tumors (Fig. 5), the 9 L tumor has a more uniform boundary around the tumor core, while the U87 tumor shows heterogeneous pH_e distribution. These results imply that the pH_e readout of each tumor type at high spatial resolution is crucial to assess the extent of tumor invasion, which may be important when assessing their responses to treatments. Moreover, the similarity between the BIRDS results in this study and those in our previous study (22) suggests that pH_e measured by BIRDS is not affected by the method used to inhibit renal clearance of the contrast agent (probenecid–$TmDOTP^{5-}$ co-infusion or renal ligation).

CONCLUSION

Our results show that probenecid–$TmDOTP^{5-}$ co-infusion can be used for intratumoral and peritumoral pH_e mapping with BIRDS.

We have demonstrated that intratumoral–peritumoral pH_e gradient mapping can be used to assess tumor invasion beyond the tumor margin. Longitudinal monitoring of pH_e from early to late stages of tumorigenesis in the same animal (to gain insights into tumor growth) is now possible with the co-infusion method. Furthermore, this method enables the assessment of therapeutic response to acidic-pH_e-targeting treatments, such as proton pump inhibitors, sodium bicarbonate, and other pH-regulating drugs (49–51).

Acknowledgements

Supported by NIH grants (R01 EB-011968, R01 CA-140102, P30 NS-052519).

REFERENCES

1. Ostrom QT, Gittleman H, Fulop J, Liu M, Blanda R, Kromer C, Wolinsky Y, Kruchko C, Barnholtz-Sloan JS. CBTRUS statistical report: primary brain and central nervous system tumors diagnosed in the United States in 2008–2012. Neuro Oncol. 2015; 17 Suppl. 4: iv1–iv62.
2. Wen PY, Reardon DA. Neuro-oncology in 2015: progress in glioma diagnosis, classification and treatment. Nat. Rev. Neurol. 2016; 12 (2): 69–70.
3. Gatenby RA, Gillies RJ. Why do cancers have high aerobic glycolysis? Nat. Rev. Cancer 2004; 4(11): 891–899.
4. Webb BA, Chimenti M, Jacobson MP, Barber DL. Dysregulated pH: a perfect storm for cancer progression. Nat. Rev. Cancer 2011; 11(9): 671–677.
5. Gerweck LE, Seetharaman K. Cellular pH gradient in tumor versus normal tissue: potential exploitation for the treatment of cancer. Cancer Res. 1996; 56(6): 1194–1198.
6. Estrella V, Chen T, Lloyd M, Wojtkowiak J, Cornnell HH, Ibrahim-Hashim A, Bailey K, Balagurunathan Y, Rothberg JM, Sloane BF, Johnson J, Gatenby RA, Gillies RJ. Acidity generated by the tumor microenvironment drives local invasion. Cancer Res. 2013; 73(5): 1524–1535.
7. Bhujwalla ZM, Artemov D, Ballesteros P, Cerdan S, Gillies RJ, Solaiyappan M. Combined vascular and extracellular pH imaging of solid tumors. NMR Biomed. 2002; 15(2): 114–119.
8. Gillies RJ, Raghunand N, Garcia-Martin ML, Gatenby RA. pH imaging. A review of pH measurement methods and applications in cancers. IEEE Eng. Med. Biol. Mag. 2004; 23(5): 57–64.
9. Lee SK. Diffusion tensor and perfusion imaging of brain tumors in high-field MR imaging. Neuroimaging Clin. N. Am. 2012; 22(2): 123–134 , ix.
10. Ludemann L, Warmuth C, Plotkin M, Forschler A, Gutberlet M, Wust P, Amthauer H. Brain tumor perfusion: comparison of dynamic contrast enhanced magnetic resonance imaging using T1, T2, and T2* contrast, pulsed arterial spin labeling, and $H_2^{15}O$ positron emission tomography. Eur. J. Radiol. 2009; 70(3): 465–474.
11. Penet MF, Artemov D, Farahani K, Bhujwalla ZM. MR-eyes for cancer: looking within an impenetrable disease. NMR Biomed. 2013; 26(7): 745–755.
12. Chen LQ, Howison CM, Jeffery JJ, Robey IF, Kuo PH, Pagel MD. Evaluations of extracellular pH within in vivo tumors using acidoCEST MRI. Magn. Reson. Med. 2014; 72(5): 1408–1417.
13. De Leon-Rodriguez LM, Lubag AJ, Malloy CR, Martinez GV, Gillies RJ, Sherry AD. Responsive MRI agents for sensing metabolism in vivo. Acc. Chem. Res. 2009; 42(7): 948–957.
14. Martinez GV, Zhang X, Garcia-Martin ML, Morse DL, Woods M, Sherry AD, Gillies RJ. Imaging the extracellular pH of tumors by MRI after injection of a single cocktail of T_1 and T_2 contrast agents. NMR Biomed. 2011; 24(10): 1380–1391.
15. Coman D, de Graaf RA, Rothman DL, Hyder F. *In vivo* three-dimensional molecular imaging with Biosensor Imaging of Redundant Deviation in Shifts (BIRDS) at high spatiotemporal resolution. NMR Biomed. 2013; 26(11): 1589–1595.
16. Coman D, Kiefer GE, Rothman DL, Sherry AD, Hyder F. A lanthanide complex with dual biosensing properties: CEST (chemical exchange saturation transfer) and BIRDS (biosensor imaging of redundant deviation in shifts) with europium DOTA-tetraglycinate. NMR Biomed. 2011; 24(10): 1216–1225.
17. Coman D, Trubel HK, Hyder F. Brain temperature by Biosensor Imaging of Redundant Deviation in Shifts (BIRDS): comparison between $TmDOTP^{5-}$ and $TmDOTMA^{-}$. NMR Biomed. 2010; 23(3): 277–285.
18. Coman D, Trubel HK, Rycyna RE, Hyder F. Brain temperature and pH measured by ^1H chemical shift imaging of a thulium agent. NMR Biomed. 2009; 22(2): 229–239.
19. Huang Y, Coman D, Ali MM, Hyder F. Lanthanide ion (III) complexes of 1,4,7,10-tetraazacyclododecane-1,4,7,10-tetraaminophosphonate for dual biosensing of pH with chemical exchange saturation transfer (CEST) and biosensor imaging of redundant deviation in shifts (BIRDS). Contrast Media Mol. Imaging 2014; 10(1): 51–58.
20. Huang Y, Coman D, Hyder F, Ali MM. Dendrimer-based responsive MRI contrast agents (G1–G4) for biosensor imaging of redundant deviation in shifts (BIRDS). Biooconjugate Chem. 2015; 26(12): 2315–2323.
21. Maritim S, Huang Y, Coman D, Hyder F. Characterization of a lanthanide complex encapsulated with MRI contrast agents into liposomes for biosensor imaging of redundant deviation in shifts (BIRDS). J. Biol. Inorg. Chem. 2014; 19(8): 1385–1398.
22. Coman D, Huang Y, Rao JU, De Feyter HM, Rothman DL, Juchem C, Hyder F. Imaging the intratumoral–peritumoral extracellular pH gradient of gliomas. NMR Biomed. 2016; 29(3): 309–319.
23. Overbosch D, Vangulpen C, Hermans J, Mattie H. The effect of probenecid on the renal tubular excretion of benzylpenicillin. Br. J. Clin. Pharmacol. 1988; 25(1): 51–58.
24. Donovan MD, O'Brien FE, Boylan GB, Cryan JF, Griffin BT. The effect of organic anion transporter 3 inhibitor probenecid on bumetanide levels in the brain: an integrated *in vivo* microdialysis study in the rat. J. Pharm. Pharmacol. 2015; 67(4): 501–510.
25. Hedaya MA, Elmquist WF, Sawchuk RJ. Probenecid inhibits the metabolic and renal clearances of zidovudine (AZT) in human volunteers. Pharm. Res. 1990; 7(4): 411–417.
26. Miyajima M, Kusuhara H, Fujishima M, Adachi Y, Sugiyama Y. Organic anion transporter 3 mediates the efflux transport of an amphipathic organic anion, dehydroepiandrosterone sulfate, across the blood–brain barrier in mice. Drug Metab. Disposit. 2011; 39(5): 814–819.
27. Sun H, Miller DW, Elmquist WF. Effect of probenecid on fluorescein transport in the central nervous system using in vitro and in vivo models. Pharm. Res. 2001; 18(11): 1542–1549.
28. Cunningham RF, Israili ZH, Dayton PG. Clinical pharmacokinetics of probenecid. Clin. Pharmacokinet. 1981; 6(2): 135–151.
29. Lasher EP, Simmons BS, Everett NB. Effects of semistarvation on the distribution of erythrocytes and plasma in organs and tissues of the rat. J. Nutr. 1958; 65(2): 317–326.
30. de Graaf RA, Chowdhury GM, Brown PB, Rothman DL, Behar KL. *In situ* 3D magnetic resonance metabolic imaging of microwave-irradiated rodent brain: a new tool for metabolomics research. J. Neurochem. 2009; 109(2): 494–501.
31. Shitara Y, Sato H, Sugiyama Y. Evaluation of drug–drug interaction in the hepatobiliary and renal transport of drugs. Annu. Rev. Pharmacol. Toxicol. 2005; 45: 689–723.
32. Hanahan D, Weinberg RA. Hallmarks of cancer: the next generation. Cell 2011; 144(5): 646–674.
33. Gabathuler R. Approaches to transport therapeutic drugs across the blood–brain barrier to treat brain diseases. Neurobiol. Dis. 2010; 37 (1): 48–57.
34. Robbins N, Koch SE, Tranter M, Rubinstein J. The history and future of probenecid. Cardiovasc. Toxicol. 2012; 12(1): 1–9.
35. Topfer M, Tollner K, Brandt C, Twele F, Broer S, Loscher W. Consequences of inhibition of bumetanide metabolism in rodents on brain penetration and effects of bumetanide in chronic models of epilepsy. Eur. J. Neurosci. 2014; 39(4): 673–687.
36. VanWert AL, Gionfriddo MR, Sweet DH. Organic anion transporters: discovery, pharmacology, regulation and roles in pathophysiology. Biopharm. Drug Disposit. 2010; 31(1): 1–71.
37. Regina A, Koman A, Piciotti M, El Hafny B, Center MS, Bergmann R, Couraud PO, Roux F. Mrp1 multidrug resistance-associated protein and P-glycoprotein expression in rat brain microvessel endothelial cells. J. Neurochem. 1998; 71(2): 705–715.
38. Strazielle N, Belin MF, Ghersi-Egea JF. Choroid plexus controls brain availability of anti-HIV nucleoside analogs via pharmacologically inhibitable organic anion transporters. AIDS 2003; 17(10): 1473–1485.

39. Robson MD, Tyler DJ, Neubauer S. Ultrashort TE chemical shift imaging (UTE-CSI). Magn. Reson. Med. 2005; 53(2): 267–274.
40. Gulaka PK, Rojas-Quijano F, Kovacs Z, Mason RP, Sherry AD, Kodibagkar VD. GdDO3NI, a nitroimidazole-based T1 MRI contrast agent for imaging tumor hypoxia in vivo. J. Biol. Inorg. Chem. 2014; 19(2): 271–279.
41. Kizaka-Kondoh S, Konse-Nagasawa H. Significance of nitroimidazole compounds and hypoxia-inducible factor-1 for imaging tumor hypoxia. Cancer Sci. 2009; 100(8): 1366–1373.
42. Barth RF, Kaur B. Rat brain tumor models in experimental neuro-oncology: the C6, 9 L, T9, RG2, F98, BT4C, RT-2 and CNS-1 gliomas. J. Neuro. Oncol. 2009; 94(3): 299–312.
43. Doblas S, He T, Saunders D, Hoyle J, Smith N, Pye Q, Lerner M, Jensen RL, Towner RA. *In vivo* characterization of several rodent glioma models by ^{1}H MRS. NMR Biomed. 2012; 25(4): 685–694.
44. Tropres I, Pannetier N, Grand S, Lemasson B, Moisan A, Peoc'h M, Remy C, Barbier EL. Imaging the microvessel caliber and density: principles and applications of microvascular MRI. Magn. Reson. Med. 2015; 73(1): 325–341.
45. Moellering RE, Black KC, Krishnamurty C, Baggett BK, Stafford P, Rain M, Gatenby RA, Gillies RJ. Acid treatment of melanoma cells selects for invasive phenotypes. Clin. Exp. Metastasis 2008; 25(4): 411–425.
46. Rofstad EK, Mathiesen B, Kindem K, Galappathi K. Acidic extracellular pH promotes experimental metastasis of human melanoma cells in athymic nude mice. Cancer Res. 2006; 66(13): 6699–6707.
47. Garcia-Martin ML, Herigault G, Remy C, Farion R, Ballesteros P, Coles JA, Cerdan S, Ziegler A. Mapping extracellular pH in rat brain gliomas *in vivo* by ^{1}H magnetic resonance spectroscopic imaging: comparison with maps of metabolites. Cancer Res. 2001; 61(17): 6524–6531.
48. McVicar N, Li AX, Goncalves DF, Bellyou M, Meakin SO, Prado MAM, Bartha R. Quantitative tissue pH measurement during cerebral ischemia using amine and amide concentration-independent detection (AACID) with MRI. J. Cereb. Blood Flow Metab. 2014; 34(4): 690–698.
49. McSheehy PM, Troy H, Kelland LR, Judson IR, Leach MO, Griffiths JR. Increased tumour extracellular pH induced by Bafilomycin A_1 inhibits tumour growth and mitosis *in vivo* and alters 5-fluorouracil pharmacokinetics. Eur. J. Cancer 2003; 39(4): 532–540.
50. Robey IF, Baggett BK, Kirkpatrick ND, Roe DJ, Dosescu J, Sloane BF, Hashim AI, Morse DL, Raghunand N, Gatenby RA, Gillies RJ. Bicarbonate increases tumor pH and inhibits spontaneous metastases. Cancer Res. 2009; 69(6): 2260–2268.
51. Silva AS, Yunes JA, Gillies RJ, Gatenby RA. The potential role of systemic buffers in reducing intratumoral extracellular pH and acid-mediated invasion. Cancer Res. 2009; 69(6): 2677–2684.

Supporting information

Additional supporting information can be found in the online version of this article at the publisher's website.